ELSEVIER

Chemical Engineering Journal 127 (2007) 11–22

Chemical Engineering Journal

www.elsevier.com/locate/cej

Modelling vortex formation in an unbaffled stirred tank reactors

G.M. Cartland Glover [a,*], J.J. Fitzpatrick [b,1]

[a] *Forschungzentrum Rossendorf, Institut für Sicherheitsforschung, P.O. Box 510119, D-01314 Dresden, Germany*
[b] *Department of Process & Chemical Engineering, University College, Cork, Ireland*

Received 9 September 2005; received in revised form 20 September 2006; accepted 23 September 2006

Abstract

Agitating liquids in unbaffled stirred tank leads to the formation of a vortex in the region of the impeller shaft when operating in the turbulent flow regime. A numerical model is presented here that captures such a vortex. The volume of fluid model, a multiphase flow model was employed in conjunction with a multiple reference frame model and the shear stress turbulence model. The dimensions of the tank considered here, were 0.585 m for the liquid depth and tank diameter with a 0.2925 m diameter impeller at a height of 0.2925 m. The impeller considered was an eight-bladed paddle type agitator that was rotating with an angular velocity of 7.54 rad s^{-1} (72 rpm) giving a Reynolds number of 10^5 and Froude number of 0.043. Preliminary results of a second investigation into the effect of liquid phase properties on the vortex formed are also presented.

Keywords: Computation fluid dynamics; Stirred tanks; Free surface vortices; Volume of fluid

1. Introduction

Stirred tanks are used across a wide spectrum of the process industry to blend fluids, dispersing two immiscible fluids (i.e. gas–liquid or liquid–liquid), to suspend solids and to promote the transport of heat and mass particularly when performing reactions. A large number of stirred tanks are designed according to "standard" or commonly used specifications, where the hydrodynamic phenomena and mixing characteristics have been widely investigated [1]. Using "non-standard" tank design will result in different fluid flow phenomena that influences the operational characteristics of the processes considered. For example removing the baffles will change the flow characteristics and therefore the mixing rate, thus altering the effectiveness of the tank design for reaction and phase contacting processes.

Suspending or dissolving solids into a liquid medium is an important process in the food industry and a significant factor is the rate at which particles sink, therefore influencing the design and operation of such stirred tanks [2]. For floating or slowly sinking particles, unbaffled stirred tanks are generally used, as the spiral flow structures that are formed, tend to draw such particles into the liquid medium [2]. These flow structures result from the rotation of the impeller that can simply be described as a primary flow rotating about the agitator shaft and a secondary flow field of two large eddies that form above and below the stirrer. The secondary vortices cause the liquid surface to be pushed up at the tank wall and sucked down near the impeller shaft. This resultant suction forms a whirlpool like vortex that entrains or draws the floating or slowly sinking solid particles into the liquid medium. Note that baffles are not generally used for the sinking of particles as the flow structures formed by the baffles suppress the development of the vortex at the impeller shaft.

To characterise the conditions required to cause the floating particle to sink, vortex formation is an important factor that is dependent on the suction rate of liquid through the impeller [2]. Vortex shape and depth is dependent on the agitation rate, the liquid medium viscosity and tank geometry. For example the depth of the impeller below the liquid surface will cause air entrainment if the impeller is close to the surface and this reduces the further away the bottom of the vortex gets from the agitator.

An investigation into the influence that the concentration of dried milk solids had on the fluid flow phenomena observed in an unbaffled stirred tank was performed [3]. The dried milk solids were added to a known volume of water that was agitated by a paddle-bladed type impeller. The dried milk solids became dissolved in the liquid phase, thus changing the physical characteristics of the liquid phase. As the dried milk solid content was increased up to a concentration of 55%, the solid–liquid

* Corresponding author. Tel.: +49 351 260 2503.
E-mail addresses: g.glover@fz-rossendorf.de (G.M.C. Glover), j.fitzpatrick@ucc.ie (J.J. Fitzpatrick).
[1] Tel.: +353 21 490 3089.

1385-8947/$ – see front matter © 2006 Elsevier B.V. All rights reserved.
doi:10.1016/j.cej.2006.09.019

Nomenclature

a	speed of sound ($m\,s^{-1}$)
arg	argument term in the SST model
B	blending function
CD	function term assessing the effect of the wall in the SST model
$\vec{f}$	continuum surface force coefficient
$\vec{F}$	continuum surface force
$\vec{g}$	gravitational acceleration vector = [0, 0, −9.81] ($m\,s^{-2}$)
k	kinetic energy ($m^{-2}\,s^{-2}$)
$\vec{n}$	interface normal vector
N	number of phases
p	pressure ($kg\,m^{-1}\,s^{-2}$)
r	volume fraction of a phase
$\vec{r}$	location vector
$\vec{S}$	source term
t	time (s)
$\vec{U}$	velocity ($m\,s^{-1}$)
y	distance to the nearest wall (m)
z	location in z-direction (m)
z_i	initial liquid height of the liquid phase (m)
z_n	unit length to non-dimensionalise the step function (m)

Greek letters

α_1	model constant for the eddy frequency equation = 5/9
α_2	model constant for the eddy frequency equation = 0.44
α_3	model constant for the eddy frequency equation
β_1	model constant for the eddy frequency equation = 0.075
β_2	model constant for the eddy frequency equation = 0.0828
β_3	model constant for the eddy frequency equation
β'	model constant for the eddy frequency equation = c_μ = 0.09
δ	interface delta function
ε	dissipation rate ($m^{-2}\,s^{-3}$)
κ	surface curvature
λ	strain rate
μ	dynamic viscosity ($kg\,m^{-1}\,s^{-1}$)
ν	kinematic viscosity ($m^2\,s^{-1}$)
ρ	density ($kg\,m^{-3}$)
σ	surface tension coefficient ($N\,m^{-1}$)
ϕ	turbulence model constant
φ_{k_1}	turbulent Prandtl number for the kinetic energy equation = 2
φ_{k_2}	turbulent Prandtl number for the kinetic energy equation = 1
φ_{k_3}	turbulent Prandtl number for the kinetic energy equation
φ_{ω_1}	turbulent Prandtl number for the eddy frequency equation = 2
φ_{ω_2}	turbulent Prandtl number for the eddy frequency equation = 1/0.856
φ_{ω_3}	turbulent Prandtl number for the eddy frequency equation
ω	turbulent eddy frequency (s^{-1})
ω'	angular velocity ($rad\,s^{-1}$)
ϕ	linear function estimating value of turbulence constants between ε and ω turbulence scales

Mathematical operators

Σ	sum operator
∂	partial differential operator
∇	Grad
∇_s	Grad over the surface
$\cdot$	dot product
$\otimes$	tensor product

Subscripts

A	air phase index
buoy	buoyancy force term
Cor	Coriolis force term
cfg	centrifugal force term
M	mass
P	phase index (for total number of phases)
rot	rotational forces for the rotating reference frame model
ref	reference value
T	transpose of the matrix
t	turbulent
W	water phase index
α	primary phase index
$\alpha\beta$	term indicating interaction between two phases
β	secondary phase index

mixture viscosity increased exponentially, particularly for concentrations greater than 40%. At the same time the liquid mixture density decreased from around $1000\,kg\,m^{-3}$ to nearly $700\,kg\,m^{-3}$ (Fig. 1A). In this state, the liquid containing the dissolved milk solids started to behave like a gel. Therefore with the change in volume and the shear regime, adjustments were made to the impeller location and agitation rate to maintain a constant vortex depth. The effect of these changes to the operation of the tank caused the particle sink time to decrease to negligible levels (Fig. 1B) [3]. This raised questions about what caused the particle sink rate to decrease so markedly, i.e. could such effects be the result of changes to the fluid properties, the increase in the suction rate of liquid through the impeller, the increase in the power consumption, changes to the flow structure (typified by the altered shape of the vortex) or as a combination of these effects.

It is proposed that a numerical model of the unbaffled stirred tank can be used to explain the change in the phenomena observed in the experimental investigation [3]. This numerical model can be implemented through the use of computational

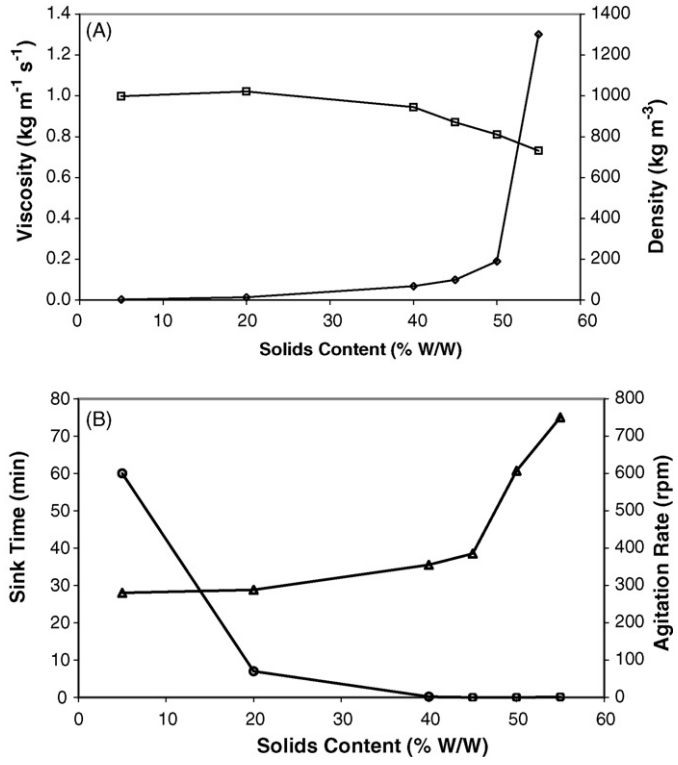

Fig. 1. Change of physical properties, particle and agitation rates with solids content in an unbaffled stirred tank reactor. (A) Viscosity (◊) (kg m^{-1} s^{-1}) and density (□) (kg m^{-3}); (B) sink time (◯) (min) and agitation rate (△) (rpm).

fluid dynamics (CFD) solvers, for example ANSYS CFX [4] or FLUENT [5] with the application of flow models that include volume of fluid, rotational flow and turbulence.

The modelling of stirred tanks has been long established to characterise rotational flow [4–21]. For the majority of numerical studies of stirred tanks the liquid surface is not considered to deform with agitation (i.e. through the use of a free-slip surface where the velocity considered is that of the fluid and not influenced by the boundary layer). The use of the free slip surface is validated by the conditions in the tank that reduce the likelihood of vortex formation (i.e. baffles [8,9,13,15,18], location, size and shape of the impeller and the tank flow regime [6–9,11–21]).

The vortex formed in the unbaffled stirred tank was numerically investigated [10,14] to good effect by achieving a close comparison with the experimental results [22]. The technique used in [10] is comparatively difficult to implement as the free surface is considered as part of the mesh. Therefore, the mesh deforms to the shape of the vortex or fluid surface as a converged solution of the flow field is calculated [10]. The numerical investigation focussed on an experimental investigation of flow structures in a 0.585 m diameter stirred tank that was agitated by an eight-bladed paddle type impeller [22]. A second numerical investigation was recently performed that utilised the volume of fluid method that applied several turbulence models (SST and various Reynolds stresses models) that reproduced the flow fields to a reasonable accuracy [14]. Axial, radial and tangential velocity profiles with secondary flow patterns were obtained from measurements made on the stirred tanks with pitot tubes [22]. The effect that these parameters had on the free liquid surface for baffled and unbaffled tanks operating under the turbulent flow regime was also discussed.

These investigations [10,14,22] provide the physical basis to validate an alternative approach to modelling the free surface of the liquid. This approach, described in the following sections, utilises both the volume of fluid and multiple reference frame techniques to assess the effect that agitation has on the formation of a vortex in an unbaffled stirred tank. The validated model is intended for use in an investigation of the effect of the change in the physical characteristics of the liquid in the flow phenomena observed when dried milk solids were added to water as described above. Initial results of this investigation are presented are also presented here.

2. Mathematical models

2.1. Fluid flow

To model the shape of the liquid surface in an unbaffled stirred tank a volume of fluid model and a multiple reference frame model are used to modify the Navier–Stokes Eqs. (1) and (2) [4].

$$\frac{\partial}{\partial t}(\rho) + \nabla \cdot (\rho \vec{U}) = \vec{S}_{\mathrm{M}} \tag{1}$$

$$\frac{\partial}{\partial t}(\rho \vec{U}) + \nabla \cdot (\rho \vec{U} \otimes \vec{U} - \mu(\nabla \vec{U} + (\nabla \vec{U})^{\mathrm{T}})) = \vec{S}_{\mathrm{M}} - \nabla \cdot p \tag{2}$$

Rotational motion is introduced to the Navier–Stokes Eqs. (1) and (2) using a multiple reference frame model. The model used here divides the tank into two separate domains, one that is rotating (in the region of the impeller) and a second that is stationary (encompassing the rest of the tank). An interface between both domains is constructed such that strict conservation of the fluxes in all equations occurs, especially with any pitch changes that occur as the rotating conditions are applied to impeller region. Additional rotational forces (Coriolis (3), and centrifugal (4), forces) that influence the flow in stirred tanks are then introduced as source terms (5), in the momentum transport equation (2) [4].

$$\vec{S}_{\mathrm{Cor}} = -2\rho\omega' \times \vec{U} \tag{3}$$

$$\vec{S}_{\mathrm{cfg}} = -\rho\omega' \times (\omega' \times \vec{r}) \tag{4}$$

$$\vec{S}_{\mathrm{M,rot}} = \vec{S}_{\mathrm{Cor}} + \vec{S}_{\mathrm{cfg}} \tag{5}$$

The volume of fluid method is used to assess the motion of the liquid being agitated in the stirred tank. This method (also known as a homogeneous multiphase flow) treats both the velocity and pressure fields as the same for all the phases considered through conditions in (6) and (7). Therefore, only one set of the Navier–Stokes equations were used to assess the flow phenomena using (1) and (2). The effect of each phase is introduced through a volume fraction equation (8), and relations that calculate the effect that the volume fraction of each phase has on the local fluid density (9), and viscosity (10). A source term (11), is

then included in (2) to account for the effect of buoyancy forces on either fluid, where ρ_{ref}, the reference density, is generally the lighter phase [4].

$$\vec{U}_\alpha = \vec{U}, \qquad 1 \le \alpha \le N_P \tag{6}$$

$$p_\alpha = p \quad \text{for all} \quad \alpha = 1, \ldots, N_P \tag{7}$$

$$\sum_{\alpha=1}^{N_P} r_\alpha = 1 \tag{8}$$

$$\rho = \sum_{\alpha=1}^{N_P} r_\alpha \rho_\alpha \tag{9}$$

$$\mu = \sum_{\alpha=1}^{N_P} r_\alpha \mu_\alpha \tag{10}$$

$$\vec{S}_{M,buoy} = (\rho - \rho_{ref})\vec{g} \tag{11}$$

To model the interface between the two fluids considered (air and water in this case), a continuum surface force model was employed. This requires the definition of a primary fluid (water) and a secondary fluid (air). Essentially, the model is a force balance that is applied to region of the interface between the phases by using Eqs. (12)–(15). Where $\delta_{\alpha\beta}$ is the interface delta function (i.e. is zero away from the interface) and $\kappa_{\alpha\beta}$ determines the curvature of the surface through the interface normal vector [4].

$$\vec{F}_{\alpha\beta} = \vec{f}_{\alpha\beta}\delta_{\alpha\beta} \tag{12}$$

$$\vec{f}_{\alpha\beta} = -\sigma_{\alpha\beta}\kappa_{\alpha\beta}\vec{n}_{\alpha\beta} + \nabla_s\sigma \tag{13}$$

$$\delta_{\alpha\beta} = |\nabla r_{\alpha\beta}| \tag{14}$$

$$\kappa_{\alpha\beta} = \nabla \cdot \vec{n}_{\alpha\beta} \tag{15}$$

2.2. Turbulence transport

As the motion of the liquid phase in the stirred tank is a fully developed turbulent flow (Reynolds number greater than 10^3), an appropriate turbulence model must be considered. Examining the flow domain, a flow separation occurs over the paddle blade impeller, therefore to model this separation accurately the shear stress transport (SST) model can be used to account for these effects. The SST model is a two-equation eddy viscosity model (16) and (17). This model differs from the k–ε turbulence and the k–ω turbulence model by employing blending functions and an alternative eddy viscosity to assess the different scales of turbulence that can be characterised by two equation models. The SST model works by estimating the region near to wall where the ω equation (17) works well in approximating the small-scale fluctuations. The model then uses relationships (18) to estimate the smaller scale fluctuations in terms of the eddy dissipation rate in the flow field away from the walls where the ε equation works well. This means that the wall conditions can be assessed automatically though the functions (19)–(26) defined below [4].

$$\frac{\partial}{\partial t}(\rho k) + \nabla \cdot (\rho \vec{U} k) = \nabla \cdot \left(\left(\mu + \frac{\mu_t}{\varphi_{k_3}} \right) \nabla k \right) + P_k - \beta' \rho k \omega \tag{16}$$

$$\frac{\partial}{\partial t}(\rho \omega) + \nabla \cdot (\rho \vec{U} \omega) = \nabla \cdot \left(\left(\mu + \frac{\mu_t}{\varphi_{\omega_3}} \right) \nabla \omega \right) + \alpha_3 \frac{\omega}{k} P_k + (1 - B_1) 2\rho \frac{1}{\varphi_{\omega_2} \omega} \nabla k \nabla \omega - \beta_3 \rho \omega^2 \tag{17}$$

$$\omega = \frac{\varepsilon}{\beta' k} \tag{18}$$

$$\phi = B_1 \phi_1 + (1 - B_1)\phi_2 \tag{19}$$

$$B_1 = \tanh(\arg_1^4) \tag{20}$$

$$\arg_1 = \min\left(\max\left(\frac{\sqrt{k}}{\beta' \omega y}, \frac{500\nu}{y^2 \omega} \right), \frac{4\rho k}{CD_{k\omega} \varphi_{\omega 2} y^2} \right) \tag{21}$$

$$CD_{k\omega} = \max\left(2\rho \frac{1}{\varphi_{\omega_2} \omega} \nabla k \nabla \omega, 1.0 \times 10^{-10} \right) \tag{22}$$

$$B_2 = \tanh(\arg_2^2) \tag{23}$$

$$\arg_2 = \max\left(\frac{2\sqrt{k}}{\beta' \omega y}, \frac{500\nu}{y^2 \omega} \right) \tag{24}$$

$$\nu_t = \frac{a_1 k}{\max(a_1 \omega, \lambda B_2)} \tag{25}$$

$$\nu_t = \frac{\mu_t}{\rho} \tag{26}$$

3. Case specifications

3.1. Tank dimensions

The experimental study of Nagata [22] included the effect of baffled and unbaffled configurations of the stirred tank in the completely turbulent flow regime using an eight-bladed paddle type impeller with a diameter of 0.2925 m, where the blade dimensions are 0.135 m × 0.06 m. The impeller (Fig. 2) was located on the centreline of a 0.585 m diameter vessel at a height of 0.2925 m from the base of the unbaffled vessel that was filled to a depth of 0.585 m with water [22]. The impeller was mounted on a shaft 0.0225 m in diameter that rotated about the vessel centreline at 72 rpm [22].

A second smaller stirred tank of diameter 0.125 m was used to investigate the effect of dried milk solids concentration on the vortex formed (Fig. 3). In this case, the impeller was mounted on a 0.0079 m diameter shaft that was moved to retain a constant depth of 0.044 m between the liquid surface and the impeller as the volume of the liquid in the stirred tank increased with the dried milk solids added [3]. The impeller was a six-bladed paddle, where the blades (0.0147 m high) were attached to a

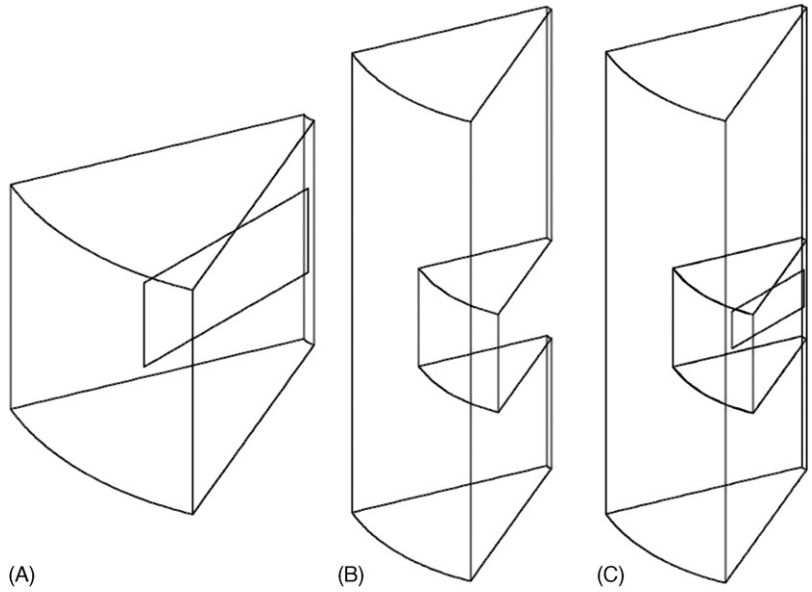

Fig. 2. Tank geometry for the Nagata case [21]. (A) Inner region; (B) outer region; (C) stirred tank with inner and outer regions in the correct locations.

0.0186 m hub to give impeller diameter of 0.0625 m [3]. For the two cases considered at 5 and 20% dried milk solids concentration the agitator was rotated at 280 and 288 rpm [3]. Note that the shaft was only located above the impeller, therefore the mesh was resolved to give to a point below the impeller as in Fig. 3 by following ideal mesh generation techniques for triangular segments [23].

3.2. Impeller region

To model the rotation of the impeller, the tank considered is split into two regions, one about the impeller and the other region is the remainder of the tank. Therefore, for the study based on the investigation of Nagata [22], a region from 0.01125 m (shaft) to 0.185 m (outer region limit) by 0.16 m high was rotated through 45° (for reasons of symmetry and computational efficiency an eighth segment of the whole tank was modelled). At the centre of the region, an internal thin wall representing the impeller was projected 0.135 m into the domain, from the shaft (see Fig. 2A). Note that the blade is 0.05 m from the edge of the impeller region in the vertical and horizontal directions. The remaining conditions include an external wall for the impeller shaft, a periodic pair interface for flow into and out of the segment and three "frozen rotor" interfaces on the surfaces lying next to the outer region (i.e. top and bottom surfaces plus the surface at 0.185 m). The frozen rotor interface condition was used to assess the flux of the rotating and stationary fluids across the boundary between the impeller and outer flow regions. Two meshes were defined

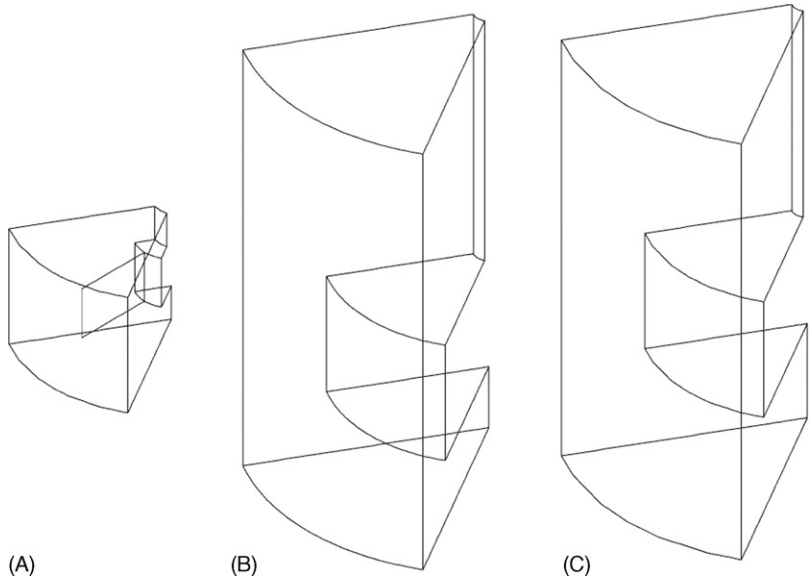

Fig. 3. Tank geometry for the dissolved dried milk solids cases [3]. (A) Inner region; (B) outer region for the 5% dried milk solids content; (C) outer region for the 20% dried milk solids content.

for the domain, a hexahedral mesh of 39,572 and a tetrahedral mesh of 22,183 elements. A rotational velocity of 7.54 rad s^{-1} or 72 rpm was applied to the fluid in this region to represent the motion of the impeller.

The impeller region for the 5 and 20% dried milk solids case was constructed in a similar fashion (Fig. 3A). However, the gap between the edge of the impeller and the blade was set to 0.01 m rather than 0.05 m and defined as a segment with an angle of 60° due to the fewer number of blades used. Seventeen thousand three hundred and sixty hexahedral elements were used to mesh the impeller region that was rotated at 280 and 288 rpm, respectively, with the interface conditions defined as above.

3.3. Outer region

The outer region of the tank based on the studies of Nagata [22] is an eighth segment of the whole tank is 0.75 m high by 0.28125 m wide from the shaft (at $r = 0.01125$ m) to the outer wall (at $r = 0.2925$ m). This mesh includes a zone above the liquid surface, so that the changes in liquid height are not impeded by the top surface of the domain). Between 0.2125 and 0.3725 m in the vertical plane and up to a radius of 0.185 m, a section of the domain is removed to allow the impeller region to be inserted (see Fig. 2B). The outer region is considered as stationary region, without application of the rotational flow equations.

Conditions applied to the domain include a rotating wall condition for the shaft (rotating at 7.54 rad s^{-1}) and a stationary outer wall for the base and the surface at 0.2925 m, as the outer region is in the stationary frame of reference. A periodic pair condition is applied to the surfaces that will interact with the other segments in vessel, and three frozen rotor interfaces to allow fluxes from the impeller region to enter the domain (i.e. the surfaces at the heights 0.2125 and 0.3725 m and at the radius of 0.185 m). An opening condition is applied to the top surface with an air volume fraction of 1 and a static pressure of 0 kg m^{-1} s^{-2} to minimise influences of the air pressure and velocity on the liquid velocity field. Note that the turbulence condition applied to the top was the default intensity and length scale. Two meshes were defined for the domain that corresponded to the meshes for the impeller region. Thus, a hexahedral mesh of 321,890 and a tetrahedral mesh of 228,104 elements were constructed.

Similar conditions were applied to outer regions (Fig. 3B and C) for the cases where the viscosity and density was modified by the addition of dried milk solid (5% and 20% dissolved milk solids). In the experiments, a constant depth between the impeller and the liquid surface was maintained [3]. This was because the density of the liquid and the mass dissolved changed with the increase in the dried milk solid content. To accommodate this change in the liquid height the height of the domain was defined as 0.125 m with a radius of 0.0625 m and an angle of 60°. The section of the tank that was removed for the impeller region was 0.03625 m in radius and 0.0347 m high and the height of the lower frozen rotor interface was changed from 0.0183 m for the 5% dried milk solids content case to 0.0283 m for the 20% case. The meshes for the 5% and 20% cases were defined with 120,826 and 119,800 hexahedral elements, respectively.

Table 1
Fluid definitions and boundary conditions

Fluids	ρ (kg m^{-3})	μ ($\times 10^3$ kg m^{-1} s^{-1})	z_i (m)
Air	1.185	0.018	–
Water	997	0.889	0.585
Water with 5% dried milk solids	998	3	0.087
Water with 20% dried milk solids	1021.4	14	0.097

3.4. Fluid conditions

To model the free surface of the liquid phase for the tank based on the experimental investigation of Nagata [22], the fluid phases were defined as air and water that both experience an operating pressure of 101325 kg m^{-1} s^{-2} and a temperature of 298 K (Table 1). The definition of the liquid phase properties for the effect of the dissolution of the dried milk solids are also found in Table 1. Note that the surface tension coefficient for the interface between the air and water phases was specified as 0.072 N m^{-1} and was assumed to remain constant for both the solids concentrations considered. This was used in the continuum-surface force model where the water phase was considered as the primary fluid.

The expressions (26)–(28) are defined to initialise the volume fraction and pressure fields prior to starting the simulation. Note that z_i is the initial liquid depth and z_n is used as a unit length to non-dimensionalise the relation for a step function to determine the local air fraction as either zero or one.

$$r_A = \text{step}\frac{z - z_i}{z_n} \tag{27}$$

$$r_W = 1 - r_A \tag{28}$$

$$p = \rho_W \times \vec{g} \times r_W(z_i - z) \tag{29}$$

3.5. Solver conditions

The specifications required to obtain a solution include the use of the steady state form of the transport equations. Second-order discretisation was specified for all the transport equations considered [4]. The under-relaxation applied to each equation was 0.1 s except for the volume fraction equation, which had an under-relaxation factor of 0.01 s for experimental study of Nagata [22] and the respective under-relaxation for the dissolved milks solids cases were 0.01 and 0.001 s. Note that the solver that was employed utilised the time-dependent term to under-relax each equation to achieve a pseudo-steady state when convergence is achieved [4]. The body force control method was selected with the averaged root mean squared type of convergence for the mean residuals set to an error of 10^{-5} to give stable values of velocity and volume fraction. This was achieved after about 650 and 1800 iterations for the hexahedral and tetrahedral Nagata cases and 6000 and 7500 iterations for the dissolved milk solids cases. The increase in the solution time was the result of the lower under-relaxation factor that was required to obtain a stable solution.

4. Results

The results of the simulations described above are presented below for the validation against the experimental investigation of Nagata [22] and the modification of the fluid properties by the dissolution of dried milk solids [3].

4.1. Nagata test case [22]

Four plots were used to depict the experimental variation of the velocity profiles in the top half of the stirred tank and show the influence that the flow structures have on the liquid surface shape [22]. The flow parameters include the tangential, axial and radial velocities with secondary flow patterns in the form of stream function contours. To compare and validate the model, field plots of the liquid surface and the secondary flow patterns (in the form of a vector field) are presented in Figs. 4 and 5. The tangential velocities for both the experimental and numerical profiles (Fig. 6) are presented next and are followed by the respective axial (Fig. 7) and radial velocities (Fig. 8).

Fig. 4 depicts the change in the liquid depth from the impeller shaft to the tank wall, as the liquid is agitated by the stirrer. The vertical and horizontal lines define the experimental limits of the liquid surface shape [22], with the radial distance of 0.12 m indicating the location at which the deformed surface crosses the initial liquid depth. The three horizontal limits indicate the depth of the bottom of the vortex (0.521 m), the initial liquid depth (0.585 m) and the depth of the liquid at the vessel wall (0.603 m). The free-surface profiles for both the hexahedral and tetrahedral cases show reasonable agreement with the experimental surface. At the vessel wall, the interface crosses the height of 0.603 m at a volume fraction of 0.8 and 0.5 for the respective meshes and at a fraction of 0.8 at 0.521 m at the impeller shaft for both cases. At 0.12 m from the impeller, where in the experimental study the gas–liquid interface crosses the initial liquid height, the volume fraction is low (less than 0.1) as the bulk of the liquid

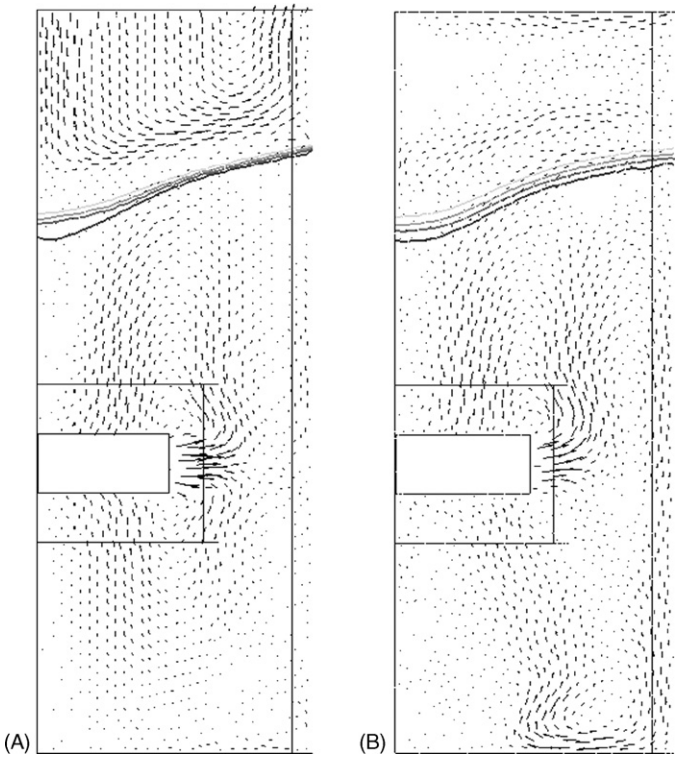

Fig. 5. Secondary flow velocity vectors in the plane of the impeller blade (i.e. at a tangent to the plane) for the hexahedral (A) and tetrahedral (B) meshes; highest velocity in the blade jet stream were 0.303 and 0.205 m s^{-1}; note that for reasons of clarity only 2000 vectors are depicted.

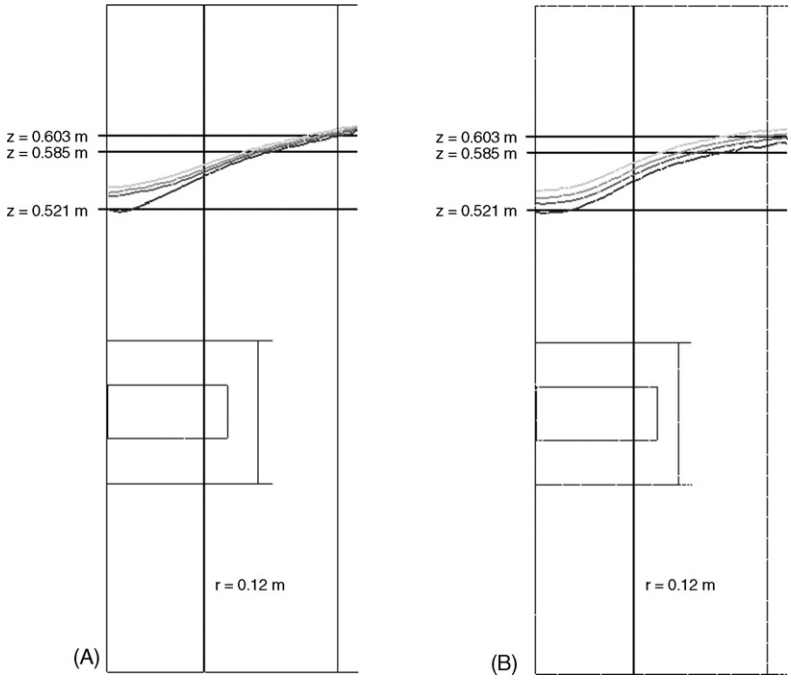

Fig. 4. Lines at $r = 0.12$ m, $z = 0.52025$, 0.585 and 0.6035 m indicate the limits of the liquid surface reported by Nagata [21]. The curved profiles are the predicted surface shape at liquid volume fractions of 0.2, 0.4, 0.6, and 0.8, between light grey and black respectively for the hexahedral (A) and tetrahedral (B) cases.

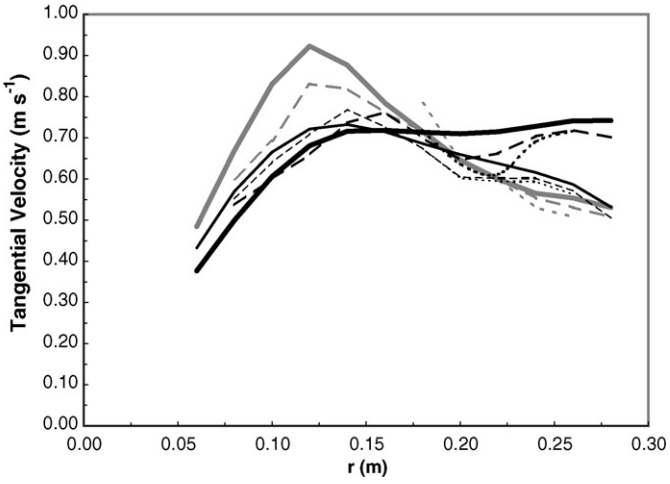

Fig. 6. Profiles of the tangential velocity ($m\,s^{-1}$) at three heights: short dashed (0.2925 m) long dashed (0.3325) and solid (0.5425 m) lines for the experimental profiles reported by Nagata [21] (thick grey lines), hexahedral meshed element domain (thick black lines) and the tetrahedral meshed domain (thin black lines).

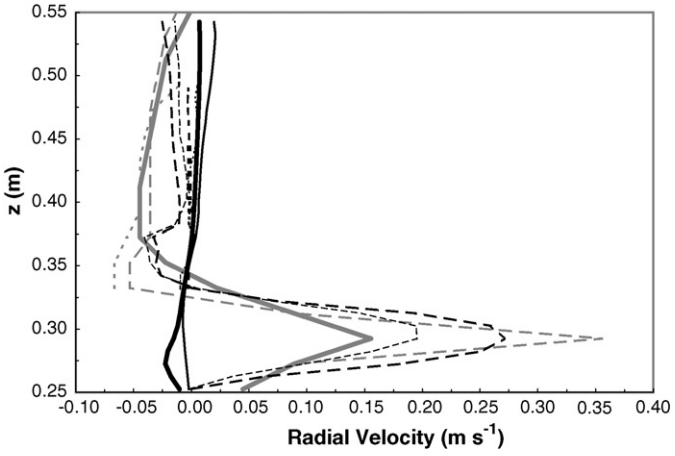

Fig. 7. Profiles of the radial velocity ($m\,s^{-1}$) at three radial positions: short dashed (0.04 m) long dashed (0.16) and solid (0.26 m) lines for the experimental profiles reported by Nagata [21] (thick grey lines), hexahedral meshed element domain (thick black lines) and the tetrahedral meshed domain (thin black lines).

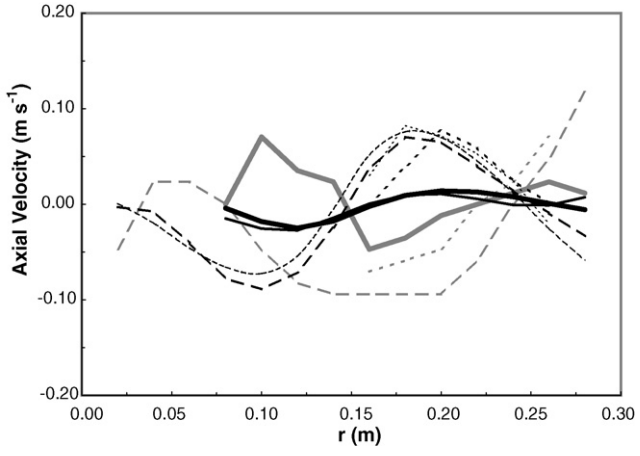

Fig. 8. Profiles of the axial velocity ($m\,s^{-1}$) at three heights: short dashed (0.3125 m) long dashed (0.3925) and solid (0.5425 m) lines for the experimental profiles reported by Nagata [21] (thick grey lines), hexahedral meshed element domain (thick black lines) and the tetrahedral meshed domain (thin black lines).

crosses over this height at a radius of up to 0.2 m for both cases. Note that the profiles found in the hexahedral case are much closer together and are not as curved as the tetrahedral case or the experimental results suggest.

Fig. 5 illustrates the vector field representation of the secondary flow profiles and on comparison with the secondary flow streamlines, it is apparent that the form of the flows are different from one another. This is apparent from the asymmetry in the tetrahedral case, as in the top half of the tank, the jet from the impeller is pointed upward whilst the hexahedral case has a jet that points horizontally to the wall with two symmetric vortices above and below the impeller. Both cases differ from the experimental streamlines [22], in that the jet appears to die out over a distance of 10 cm for the simulations, whilst the vortex above the impeller is observed to reach the wall for the experimental study. This feature of the flow is consistent with later investigations [6–21]. However, it must be noted that the tank configuration modelled in [21] is markedly different with three impellers agitating the liquid. Other vortices are formed between the where the jet dies out and the tank wall and both effects suggest that there is an imbalance in the energy imparted into the flow by the impellers. The effect of this is to limit the formation of the large-scale vortices that influence the flow structure both above and below the impeller. The effect that this has on the velocity profiles in the upper half of the tank can be observed (Figs. 6–8).

Fig. 6 depicts the tangential velocity profiles for both the experimental and numerical investigations, respectively. A single peak is observed for the experimental profiles above the impeller at a radius of 0.12 m, where maximum velocities of 0.8–0.9 $m\,s^{-1}$ were observed. A singular peak is also observed for the profiles with the tetrahedral meshed case, but the location of the peaks are found between 0.14 with maximum velocities of up to 0.76 $m\,s^{-1}$, therefore under-predicting the velocities by up to 0.2 $m\,s^{-1}$. However, the hexahedral case is different in that there is no significant peak, as the velocities are of the same order of magnitude near to the wall.

Better agreement between the experimental and numerical flow profiles is apparent in the radial velocities in the region close to the impeller (Fig. 7). However, peak velocities in the stream away from the impeller are 0.09 and 0.17 $m\,s^{-1}$ for the hexahedral and tetrahedral cases. The under-prediction in the velocities for the tetrahedral case can be explained by the angle of the flow stream away from the blade tip (with respect to the horizontal axis) as between 20° and 30° (see Fig. 5) so that a significant proportion of these vectors is also found in the axial direction. This differs from the experimental data and hexahedral case where horizontal jets are depicted.

The axial profiles for the simulations presented in Fig. 8 do not correspond to the experimental velocities. The reason why can be explained by the differences observed in the jet from the impeller dying out in the middle of the tank as depicted in Figs. 5 and 7, the effect of this influences the flow structures in the rest of the tank. It must be noted that even though the structural differences are apparent, velocities of a similar magnitude are observed for both cases and this has a small influence on the shape of the free surface. It is possible to compare the profiles in

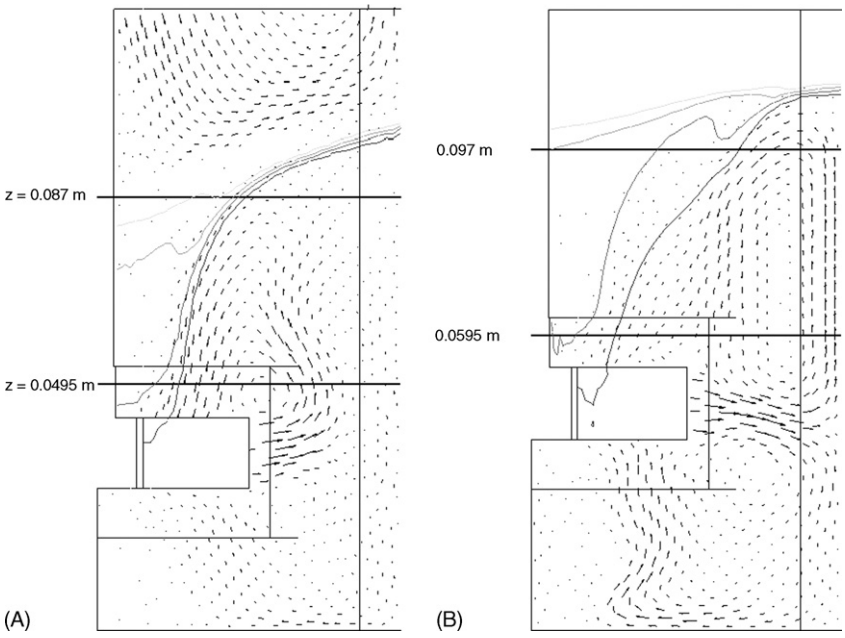

Fig. 9. Velocity vector field and volume fraction contours of the 5% (A) and 20% (B) dissolved milk solids mixture, where the limits indicate the initial liquid height and the measured depth of the vortex. Highest velocities in the blade jet stream were 0.266 and 0.342 m s^{-1} respectively. Surface profiles at volume fractions of 0.2, 0.4, 0.6, and 0.8, between light grey and black, respectively.

Fig. 8 with the axial profiles presented in [11,12] for both experimental and numerical systems under conditions of laminar flow. Similarities were observed in the shape of the profiles, though no quantitative comparisons can be made as the cases considered are very different due to the tank geometries considered.

4.2. Dried milk solids cases [3]

The flow fields from the initial simulations of the experimental study described above, where dried milk solids were dissolved in a litre of water up to concentration of 55% dissolved milk solids are presented in Fig. 9. The meshes for both these cases are hexahedral in form, as the flow in both the upper and lower halves of the tank was found to be more symmetrical for the hexahedral case study based on the experiments of Nagata [22]. Another reason was that the free surface of the hexahedral case was also more compact than the tetrahedral case. Nevertheless, the flow structures in the liquid were not reproduced as accurately as is possible, the phenomena in the region of the free surface is still good enough for further application particularly as the tank considered here is considerably smaller in scale (diameter of 0.125 m compared to 0.585 m). Thus, it is possible to determine the flow conditions that influence the sinking of dried milk particles before they can be dissolved. Note that in these simulations it was assumed that the dried milk solids were completely dissolved. Therefore, the solid particles had no influence on the flow structures in the tank.

The free surface profiles for both the 5 and 20% dissolved milk solids cases depicted in Fig. 9 display a sharp gradient for the fractions of 0.6 and 0.8 between the initial liquid height (0.087 and 0.097 m) and the base of the vortex (0.0495 and 0.0595 m). The lower fractions of 0.2 and 0.4 have a shallower gradient that is comparable to the liquid that is found above the initial liquid height. However, the gradient in the free-surface elevation is lower for the 20% dissolved solids cases.

The major difference between both cases is that the jet of liquid from the impeller blade is angled upwards at around 10° and quickly dies out for the 5% case. The 20% case is angled downwards at around 10° and the jet reaches the tank wall. For the 5% case there are two secondary flow vortices above the impeller, with the stronger velocities observed in the eddy next to the deformed surface generated by the liquid flow, whilst only a single vortex appears above the impeller in the 20% case. The differences in the observed flow structures cause the differences in the form of the predicted free surface profiles.

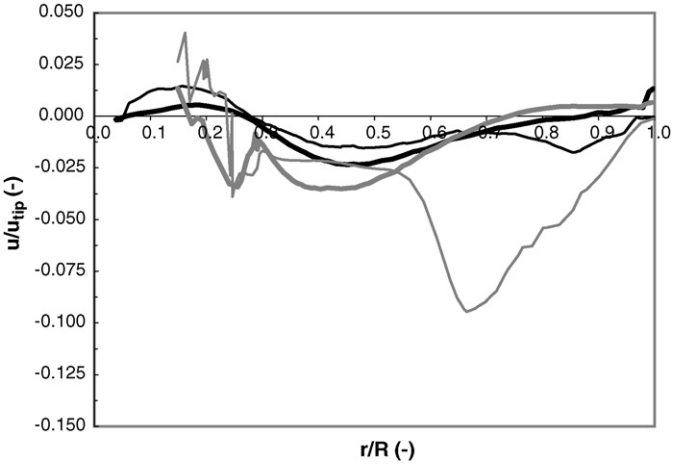

Fig. 10. Profiles of the radial velocities at the free surface location corresponding to the liquid volume fraction of 0.8 for the both hexahedral (thick black line) and tetrahedral (thin black line) meshes with Nagata and the 5% (thick grey line) and 20% (thin grey line) dissolved milk solids cases. Note that there is non-dimensionalisation with respect to the tank radii and the impeller tip speeds.

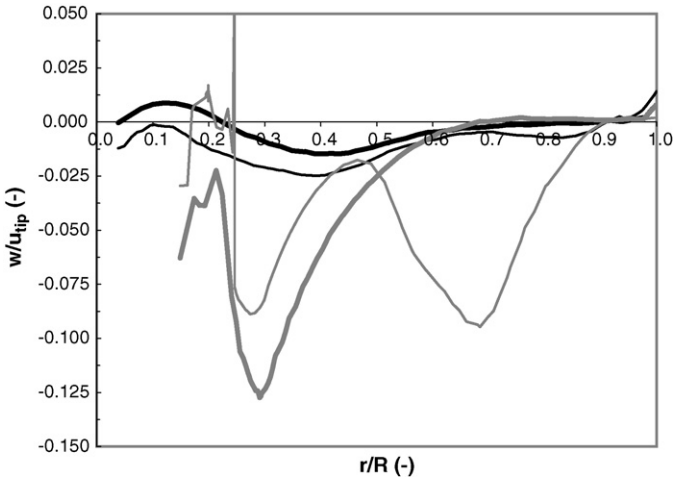

Fig. 11. Profiles of the axial velocities at the free surface location corresponding to the liquid volume fraction of 0.8 for the both hexahedral (thick black line) and tetrahedral (thin black line) meshes with Nagata and the 5% (thick grey line) and 20% (thin grey line) dissolved milk solids cases. Note that there is non-dimensionalisation with respect to the tank radii and the impeller tip speeds.

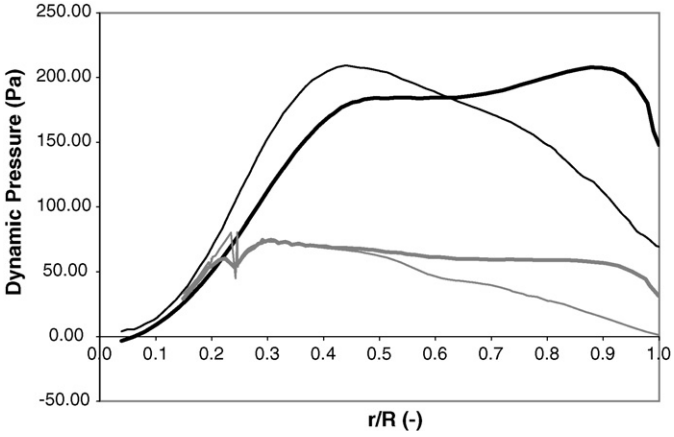

Fig. 12. Profiles of the dynamic pressures at the free surface location corresponding to the liquid volume fraction of 0.8 for the both hexahedral (thick black line) and tetrahedral (thin black line) meshes with Nagata and the 5% (thick grey line) and 20% (thin grey line) dissolved milk solids cases. Note that there is non-dimensionalisation with respect to the tank radii.

4.3. Comparison of flow variables between numerical cases

The structure of the free surfaces for all the cases shows the captures quantitatively the physicality of the phenomena observed in experiments if not qualitatively. Therefore, insight into the sinking characteristics observed in milks solid study can be obtained from examining the liquid velocities and the pressures (Figs. 10–12).

Fig. 10 depicts the radial velocities at the free surface. For most of the tank radius the observed velocities are negative (i.e. the liquid velocity component is pointing towards the impeller). This suggests that particles would be moved in the direction of the impeller. However, for both the hexahedral and tetrahedral cases of the Nagata [22] study and the 5% dissolved milk solids these velocities are small (>-0.04), suggesting that this effect is not strong. Yet for the 20% solids case the observed velocity component has a stronger velocity (nearly -0.10) closer to the tank wall. Referring back to Fig. 1, it was observed that there was a strong reduction in the sink time between the 5 and 20% dried milk solids cases, for an apparently small change in physical properties, geometrical configuration and agitation rate. Therefore, this difference between the two profiles could help explain the change in the sink times observed.

Examining the axial velocity profiles in Fig. 11 at the free surface of both the hexahedral and tetrahedral meshed cases of the experimental study Nagata [22], the profiles are similar to measured profiles. Therefore, the earlier supposition that the flow structures are broadly correct is backed up by these profiles. However, caution must be used as these profiles are not found in the rest of the tank and that the velocities observed here are fairly small at $<|0.025|$. In the case of the 5 and 20% solids cases, the velocities are much higher in magnitude, with a strong peak at a third of the radius for both dissolved milk solids cases that correspond to the strong change the liquid surface. A second peak in the axial velocity is also observed for the 20%

Table 2
Flow parameters extracted from the surface zones on the impeller region

Case	Surface on the impeller zone	Area (m^2)	Area averaged velocity ($m\,s^{-1}$)	Area integrated velocity ($\times 10^3\ m^3\,s^{-1}$)	Mass flow rate ($kg\,s^{-1}$)	Total pressure in stationary frame (Pa)
	Base	0.0134	0.664	8.88	0.333	3664
Tetrahedral (Nagata)	Top	0.0134	0.672	8.99	0.106	2103
	Wall	0.0232	0.688	15.59	−0.439	3115
	Base	0.0151	0.680	10.26	0.193	3688
Hexahedral (Nagata)	Top	0.0151	0.683	10.29	0.131	2125
	Wall	0.0247	0.675	16.65	−0.325	3131
	Base	0.0009	0.481	0.43	0.0223	700
Five percent solids	Top	0.0009	0.493	0.43	0.0167	379
	Wall	0.0015	0.480	0.72	−0.0396	643
	Base	0.0009	0.458	0.41	0.0546	730
Twenty percent solids	Top	0.0009	0.409	0.36	0.0555	395
	Wall	0.0015	0.426	0.64	−0.1104	651

case at approximately two thirds of the radius. The velocities show that there is a greater suction force that would act on dried milk particles when they are added to the liquid. However, it is important to note that the velocities at a dimensionless radius of less than 0.25 correspond to the region where the 80% fraction contour corresponds to the location of the impeller as seen in Fig. 9.

Fig. 12 depicts the dynamic pressures observed at the free surface. The profiles have two forms, with a peak at 0.3–0.4 of the tank diameter for all cases. However, in two cases the pressure reduces as the radius is increased (tetrahedral mesh case and the 20% solids case) and for the other two cases there is a second peak close to the wall with a plateau in between. Therefore, little can be derived from the impact of the dynamic pressure on the flow phenomena in the dried milk solids cases as a result of the profiles observed here.

Further effects to elucidate influences on the surface formation and the particle sink rate may be obtained from flow rates into and out of the impeller region and the pressures acting on the liquid at locations between the impeller and the liquid surface (Table 2). Between the two cases based on the studies of Nagata [22], differences arise from the area integrals of the meshes, as the hexahedral mesh has larger cross-sectional areas. Yet the velocities, the volume and mass flow rates are not significantly different. For the dissolved milk solids cases, the only noticeable difference is in the mass flow rates, which is a result of the change in the physical properties of the mixtures. Note that the negative value for the wall value corresponds to mass leaving the impeller zone.

5. Conclusions

A reasonable representation of the flow phenomena in an unbaffled stirred tank operating in the turbulent flow regime was achieved using a volume of fluid multiphase model in conjunction with a multiple reference frame model. Therefore, the technique discussed was used to assess the impact that fluid properties have on the fluid flow phenomena observed when dried milk solids are added to a liquid at concentrations of 5 and 20% in a much smaller tank. Where changes to the local pressures and flow rates can indicate the causes behind the reduction of particle sink times that were observed experimentally [3]. The results indicate that even with a small change in the physical properties observed between the 5 and 20% cases a significant change in the radial and axial velocities at the free surface are observed.

Some questions remain over the accuracy of the technique used due to the significant differences observed in the axial velocity profiles for the experimental and numerical cases. To improve the accuracy of the modelling techniques, it would be prudent to investigate the phenomena in a similar vessel operating under the turbulent flow regime by exploiting the advances in experimental techniques since the original investigation was performed (i.e. Laser Doppler Anemometry and Particle Image Velocimetry). Enhancements that could be made to the numerical model would include considering the whole domain (all 360° of the tank, rather than a 45° or 60° segment [14,19]) and the use of an alternative turbulence modelling techniques. Such techniques considered include large eddy, detached eddy or scale adaptive simulations or the Reynolds stress model that would improve calculation of turbulence in the flow field. This is especially important in the estimating the turbulent energies in flow-stream moving away from the impeller and particularly for cases considering larger tanks [6–10,14,16,17]. Further validation would include the modelling an unbaffled stirred tank operating under a regime without significant surface deformation [11,12]. This would be a good test to observe whether or not the volume of fluid model is influenced by the flow structures that were depicted here in such system where the liquid surface is not affected by the hydrodynamics.

Acknowledgements

We would like to acknowledge the support of the EU through Marie Curie sponsorship of the research (Contract number HPMD-CT-2000-00020) and Ansys CFX Limited for enabling this work to be presented.

References

[1] J.M. Coulson, J.F. Richardson, J.R. Backhurst, J.H. Harker, Chemical Engineering, vol. 1 (Fluid Flow, Heat Transfer and Mass Transfer), Pergamon Press, Oxford, 1990.
[2] B. Freudig, S. Hogekamp, H. Schubert, Dispersion of powders in liquids in a stirred vessel, Chem. Eng. Process. 38 (1999) 525.
[3] J.J. Fitzpatrick, N. Weber, C. Schober, K. Weidendorfer, E. Teunou, Effect of viscosity and vortex formation on the mixing of powders in water to form high concentration solutions in stirred-tanks, in: Proceedings of the Fourth World Congress on Particle Technology, Sydney, Australia, 2002.
[4] ANSYS Incorporated, ANSYS CFX Release 10.0 Documentation, ANSYS Incorporated, Cannonsburg, PA, USA, 2005.
[5] Fluent Incorporated, User Guide, Fluent Incorporated, Lebanon, New Hampshire, USA, 2003.
[6] A.H. Alexopoulos, D. Maggioris, C. Kiaparissides, CFD analysis of turbulence non-homogeneity in mixing vessels: a two compartment model, Chem. Eng. Sci. 57 (2002) 1735.
[7] P. Armenante, C.-C. Chou, R.R. Hemrajani, Comparison of experimental and numerical fluid viscosity distribution profiles in an unbaffled mixing vessel provided with a pitched-blade turbine, Institut. Chem. Eng. Sympos. Ser. 136 (1994) 349.
[8] A. Brucato, M. Ciofalo, F. Grisafi, G. Micale, Numerical prediction of flow fields in baffled stirred vessels: a comparison of alternative modelling approaches, Chem. Eng. Sci. 53 (1998) 3653.
[9] A. Brucato, M. Ciofalo, F. Grisafi, R. Tocco, On the simulation of stirred tank reactors via computational fluid dynamics, Chem. Eng. Sci. 55 (2000) 291.
[10] M. Ciofalo, A. Brucato, F. Grisafi, N. Torraca, Turbulent flow in closed and free-surface unbaffled tanks stirred by radial impellers, Chem. Eng. Sci. 51 (1996) 3557.
[11] L. Dong, S.T. Johansen, T.A. Engh, Flow induced by an impeller in an unbaffled tank. I. Experimental, Chem. Eng. Sci. 49 (1994) 549.
[12] L. Dong, S.T. Johansen, T.A. Engh, Flow induced by an impeller in an unbaffled tank. II. Numerical modelling, Chem. Eng. Sci. 49 (1994) 3511.
[13] D. Gobby, Mixing of Newtonian and non-Newtonian fluids in an agitated baffled tank. CFX Validation Report CFX-VAL12/1202. Oxford, CFX Limited, 2002.
[14] J.N. Haque, T. Mahmud, K.J. Roberts, Modeling turbulent flows with free-surface in unbaffled agitated vessels, Industr. Eng. Chem. Res. 45 (2006) 2881.

[15] R.M. Jones, A.D. Harvey, S. Acharya, Two-equation turbulence modelling for impeller stirred tanks, J. Fluids Eng. Transact. Am. Soc. Mech. Eng. 123 (2001) 640.
[16] G. Montante, K.C. Lee, A. Brucato, M. Yianneskis, Numerical simulations of the dependency of flow pattern on impeller clearance in stirred vessels, Chem. Eng. Sci. 56 (2001) 3751.
[17] L. Mununga, K. Hourigan, M. Thompson, Numerical study of the effect of blade sze on pumping effectiveness of a paddle blade impeller in an unbaffled mixing vessel, in: Proceedings of the Third International Conference on CFD in the Minerals and Process Industries, CSIRO, Melbourne, Australia, 2003.
[18] V.V. Ranade, An efficient computational model for simulating flow in stirred vessels: a case of Rushton turbine, Chem. Eng. Sci. 52 (1997) 4473.
[19] R. Verzicco, G. Iaccarino, M. Fatica, P. Orlandi, Flow in an impeller stirred tank using an immersed boundary method, AIChE J. 50 (2004) 1109.
[20] F. Wang, W. Wang, Y. Wang, Z.-S. Mao, CFD Simulation of solid liquid two-phase flow in baffled stirred vessels with Rushton turbines, in: Proceedings of the Third International Conference on CFD in the Minerals and Process Industries, CSIRO, Melbourne, Australia, 2003.
[21] J.M. Zalc, E.S. Szalai, M.M. Alvarez, F.F. Muzzio, Using CFD to understand chaotic mixing in laminar stirred tanks, AICHE J. 48 (2002) 2124.
[22] S. Nagata, Mixing: Principles and Applications, Wiley, New York, 1975.
[23] ANSYS Incorporated, ICEM CFD Release 10.0 Documentation, Ansys Incorporated, Cannonsburg, PA, USA, 2005.